J Radioanal Nucl Chem (2015) 306:457–467
DOI 10.1007/s10967-015-4097-2

Nuclear forensic applications involving high spatial resolution analysis of Trinitite cross-sections

Patrick H. Donohue[1] · Antonio Simonetti[1] · Elizabeth C. Koeman[1] · Sara Mana[1,2] · Peter C. Burns[1,3]

Received: 22 January 2015 / Published online: 3 April 2015

Abstract This study reports a comprehensive cross-sectional analysis of major and trace element abundances and $^{240}Pu/^{239}Pu$ ratios within vertically oriented Trinitite thin sections. The upper glassy layer ($\sim$2 mm thick) represents fused desert sand combined with devolatilized fallout from the debris cloud. The vertical distribution of $^{240}Pu/^{239}Pu$ ratios indicates that residual fuel was incorporated deeper (up to $\sim$10 mm depth) into Trinitite than previously reported. This requires thorough mixing and disturbance of the upper cm of the blast site prior to or during the initial melting of the desert sand resulting from the nuclear explosion.

Keywords Nuclear forensics · Trinitite · Laser ablation · Post-detonation material

Introduction

Nuclear proliferation and expanding access to nuclear technology has increased the potential of a nuclear incident or unauthorized detonation [1, 2]. Such an event would create post-detonation material (PDM) containing mixed major and trace element and isotopic characteristics from both the nuclear device and impacted environment. Indeed, tens of thousands of tons of PDMs were generated prior to the worldwide ban on nuclear testing [3]. Characterizing nuclear explosion processes and their effects on the surrounding environment is a major objective of nuclear forensics. Developing methods for rapid and accurate source attribution may help to deter such incidents. However, the chemical and isotopic signatures in PDMs are apparently heterogeneously distributed [e.g., 4, 5], which may result in inaccurate interpretations. For example, the heterogeneous distribution of Ba and Cs in PDMs, used in blast yield calculations, can lead to variable and improbable yield estimates [6]. Thus, the nature of PDM sample collection and analysis must be carefully considered in order to develop the most effective strategies for obtaining accurate forensic information.

One effective avenue for developing nuclear forensic strategies is investigating historical PDMs, such as Trinitite. The latter was chosen because it is a relatively well-characterized PDM since the bomb design and isotopic composition of the nuclear fuel used in the explosion are known [7–9], and it formed in a geologically simple environment [10]. The arkosic sand in the desert at ground zero (GZ) included quartz, feldspars (K- and Na-rich end-members), carbonates, sulfates, chlorides, zircon, hornblende, olivine, monazite, apatite, magnetite, ilmenite, augite, and illite [4, 9, 11–13]. Bellucci et al. [4] determined the major and trace element composition of Trinitite is influenced primarily by incipient melting of the local arkosic sand and incorporation of anthropogenic components (e.g., blast tower, bomb material).

The nuclear device ("Gadget") exploded at Trinity was an implosion-type plutonium bomb, with tamper shells of

Electronic supplementary material The online version of this article (doi:10.1007/s10967-015-4097-2) contains supplementary material, which is available to authorized users.

✉ Patrick H. Donohue
pdonohu1@alumni.nd.edu

[1] Civil & Environmental Engineering & Earth Sciences, University of Notre Dame, Notre Dame, IN 46556, USA

[2] Department of Earth and Environmental Sciences, University of Iowa, 121 Trowbridge Hall, Iowa City, IA 52242, USA

[3] Department of Chemistry and Biochemistry, University of Notre Dame, Notre Dame, IN 46556, USA

U and Be [7]. The aerial extent of Trinitite was non-uniform, but extended ~370 m radially away from GZ [14]. The intense heat (>1000 K at GZ, >8000 K in the fireball [3]) from the blast was short lived, as the ambient ground temperature was rapidly cooled by air driven inward by updrafts. However, there is evidence for melt flow and settling during this brief time [9, 15]. Glass thickens at the base of slopes facing GZ [10], and thin section element maps show regions of Si-, Ca-, and K-rich melt [4]. In addition, vesicle morphology indicates Trinitite remained in a molten or semi-molten state long enough for vesicles to partially coalesce and deform.

The uppermost region of the desert sand was irradiated during the blast, and fallback particles subsequently increased the surface concentration of radioactivity, as demonstrated by alpha track radiography and beta spectroscopy [e.g., 16]. The activities of γ-emitting particles (e.g., ^{241}Am, ^{152}Eu) are similar for both the glassy and sandy sides of Trinitite [17]. High-activity regions are typically the focus of forensic investigations, as they are considered most likely to reveal bomb-like signatures [16, 17]. The ^{240}Pu/^{239}Pu ratio of Gadget is calculated to be 0.0129 ± 0.003 [8]. Previous in situ studies of Trinitite report ^{240}Pu/^{239}Pu ratios between 0.012 and 0.026 [4, 16, 18], signatures consistent with super-grade Pu fuel used by Gadget (<3 % ^{240}Pu by weight) [8]. Sharp et al. [18] performed an analytical transect through a vertical thin section of Trinitite and found weapons grade Pu signatures at ~1.5 mm depth.

Previous investigations of Trinitite have focused on: *1*—documenting the nature of bomb-related inclusions found on blast melt surfaces [19]; *2*—determining the abundances of radionuclides (fission and activation products and isotopic composition of Pu) [16]; *3*—characterizing the U [20] and Pb [21] isotope systematics; and *4*—reporting the oxygen isotope compositions [13]. These previous studies have used bulk sample analysis [e.g., 13, 22], or have involved detailed investigations conducted at high spatial resolution (10–100 s micron scale; e.g., [4, 20, 21]). However, in the case of the latter, the location of spot analyses within Trinitite petrographic thin sections were dictated primarily by identifying areas of high alpha particle emissions (regions rich in U and/or Pu) within Trinitite as revealed by alpha radiography (e.g., [16]; Fig. 1). Thus, detailed, high spatial resolution investigations of individual Trinitite samples, such as conducting systematic (vertical) traverses across samples, were not carried out.

Therefore, the purpose of this work is to investigate the chemical (major and trace element abundances) and Pu isotopic compositions within vertical cross-sections of Trinitite at high spatial resolution (<100 microns) using standard petrographic thin sections to obtain a better understanding of the formational history of Trinitite. This study is the first comprehensive characterization of trace element abundances and Pu isotopic measurements of Trinitite glass with depth. It is hypothesized that the near-surface (upper few millimeters) geochemistry in Trinitite will reflect a greater contribution from the nuclear device and infrastructure components present at GZ (e.g., Fe, Pu, U). Many of the physical dynamics of the blast (i.e., the interaction between device-related forces and the surrounding geology) are recorded in Trinitite. The resulting vertical distributions of radionuclides are likely related to post-detonation formation and transport mechanisms of nuclear and natural materials subsequent bomb detonation.

Samples

Three vertical-cut thin Sections (4D 9.18, 4F 8.86, and 5A 8.86) and one oblique-cut section (relative to the horizontal surface; 5A 6.06) were selected from our sample collection using multiple criteria to verify orientation. For example, vertical-cut thin sections transition from an upper glassy layer to a coarser-grained base (Fig. 1). The oblique-cut section from sample 5A 6.06 also exhibits this transition (Fig. 1g, h). The sample naming convention for Trinitite [c.f., 20] groups samples by morphology or notable characteristics, followed by the original sample weight. This classification scheme allows a first order separation of sample types based on sample shape or the presence of surface inclusions. The sample types in this study include the following groups: 4D, unusual blue inclusions; 4F, glassy blue-green inclusions, thought to originate from quartz; and two 5A types, which have a dark surface and lighter-colored glass base. Samples were classified by and purchased from a commercial provider (Mineralogical Resource Co.; http://www.minresco.com).

Trinitite was removed from GZ and buried in 1952 to reduce environmental risk [8], thus few samples exist that were collected in situ. Variations in ^{152}Eu activity, which is highest at GZ, have been used to calculate original distances from the blast [8, 22]. For the samples investigated here, the calculated distances range from 51 ± 2 m (samples 5A 6.06, 5A 8.86) to 68 ± 7 m (sample 4D 9.18) [22]. The ^{152}Eu activity of sample 4F 8.86 was too low to yield a reliable distance calculation [22].

Additional characteristics such as alpha track concentration and major element maps (Fig. 1) were used for planning vertical transects. A typical vertical section of Trinitite has an alpha track density highest at the upper surface, with little to none in the substrate. Vertical transect spot analyses were conducted along relatively continuous and tightly constrained paths with minimal vesicles (Fig. 1). Regions (≳75 μm) of continuous glass that are

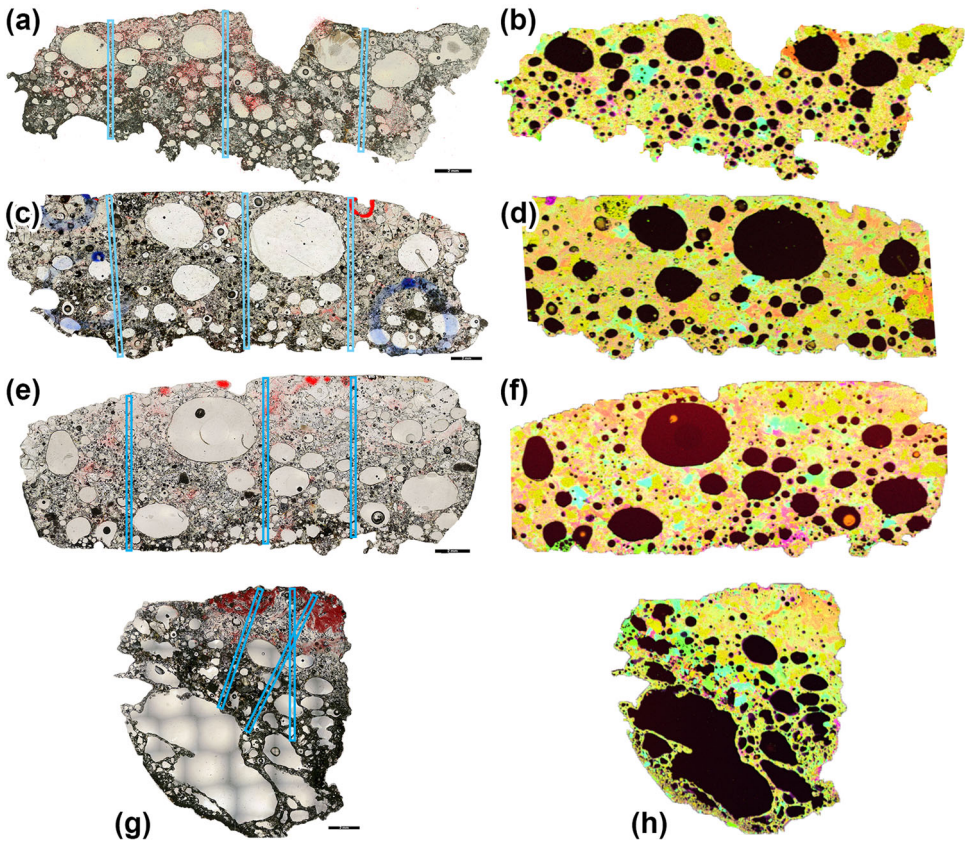

Fig. 1 *Left column* Sample microphotograph mosaics in plane polarized light, overlain by alpha tracks (*red*) to highlight high alpha-activity regions, and spot analyses in transects conducted here (*blue rectangles*). Trinitite sections are oriented with glassy (*blast melt*) surfaces at the top; *Right column* Micro-XRF element map mosaics of Si (*yellow*), Ca (*red*), Al (*green*), K (*cyan*), and Fe (*purple*) for respective samples. Samples are 4D 9.18 (**a**, **b**); 4F 8.86 (**c**, **d**); 5A 8.86 (**e**, **f**); and 5A 6.06 (**g**, **h**). *Scale bar* is 2 mm

free of vesicles and unmelted (precursor) mineral grains were selected for laser ablation analysis in order to minimize the contribution of the latter and hence not bias the determined trace element abundances.

Methodology

Imaging

Thin sections were imaged at 5× magnification and images were composited in Adobe© *Photoshop*©. The resulting photomosaics have resolutions of ~33 pixels per 0.05 mm. Spatially resolved alpha track radiography [c.f., 17] was conducted using methods described in Wallace et al. [16]. Alpha tracks were imaged and mosaicked using the same process as for sample microphotographs, and subsequently overlain onto the sample to identify high alpha activity regions.

Semi-quantitative major element maps were constructed using an EDAX Orbis Micro Energy Dispersive X-Ray Fluorescence (μ-XRF) system (EDAX Inc., Mahwah, NJ, USA). Operating conditions are summarized in Table 1. The voltage (35–40 kV) and amperage (250–350 μA) were adjusted to yield >10,000 counts and between 30 and 50 % deadtime for a 30 μm beam size. The resulting major element maps (~20–50 microns/pixel resolution) were used to qualitatively assess sample heterogeneity along vertical transects. This was supplemented by scanning electron microscope (SEM) and back scattered electron (BSE) images obtained using an EVO 50 Zeiss environmental SEM equipped with an Oxford Instrument energy-dispersive X-ray analyzer at the Notre Dame Integrated Imaging Facility.

Electron microprobe (EMP) analysis

Abundances of major and minor elements (Si, Ca, Al, K, Fe, Mg, Na, Mn, and Ti) in Trinitite glass were obtained using a Cameca SX50 EMP at the University of Chicago (Chicago, Illinois). Operating conditions were 15 kV accelerating potential and 30 nA probe current with a 15 μm spot size. The larger spot size was used to minimize volatilization of Na and K, and reduce the effects of local heterogeneities on element determination. Selected regions of analysis were chosen based on homogeneity (as interpreted from BSE and μ-XRF images) for distances ≳75 μm from EMP points for subsequent LA-ICP-MS investigation. Relict quartz grains (areas identified as containing >90 % SiO_2) were avoided during analysis.

Table 1 Analytical settings

EDAX Orbis Micro EDXRF	
X-ray aperture	30 μm
Voltage	35–40 kV
Amperage	250–350 μA
Amp time	12.8 μs
Matrix size	512 × 400
Resolution	20–50 μm/px
Dwell time	100 μs
Spectrum map	32-bit
Acquisition time	6.5 h
NewWave UP213 LA-ICP-MS and *ThermoFinnigan Element 2 ICP-MS*	
Laser type	Nd:YAG
Brand	New Wave Research
Wavelength	213 nm
Pulse duration	5 ns
Spot size	40 μm
Repetition rate	5 Hz
Fluence	10–12 J cm^{-2}
Resolution mode	Low
Scan mode	E-scan
Scanned masses	^{43}Ca, ^{47}Ti, ^{53}Cr, ^{55}Mn, ^{56}Fe, ^{59}Co, ^{60}Ni, ^{63}Cu, ^{65}Cu, ^{64}Zn, ^{66}Zn, ^{67}Zn, ^{68}Zn, ^{69}Ga, ^{71}Ga, ^{85}Rb, ^{86}Sr, ^{89}Y, ^{90}Zr, ^{92}Zr, ^{93}Nb, ^{99}Tc, ^{100}Ru, ^{101}Ru, ^{102}Ru, ^{104}Ru, ^{117}Sn, ^{126}Te, ^{133}Cs, ^{137}Ba, ^{138}Ba, ^{139}La, ^{140}Ce, ^{141}Pr, ^{147}Nd, ^{147}Sm, ^{149}Sm, ^{152}Sm, ^{154}Sm, ^{151}Eu, ^{153}Eu, ^{160}Gd, ^{159}Tb, ^{163}Dy, ^{165}Ho, ^{166}Er, ^{169}Tm, ^{172}Yb, ^{175}Lu, ^{180}Hf, ^{181}Ta, ^{184}W, ^{206}Pb, ^{207}Pb, ^{208}Pb, ^{232}Th, ^{233}U, ^{234}U, ^{235}U, ^{236}U, ^{238}U, $^{239-242}$Pu, ^{244}Pu
External standard	NIST SRM 612
Data reduction software	GLITTER©

Standardization was performed using well-characterized in-house standards of manganese hortonolite (SiO_2, FeO, MgO, MnO), anorthite (CaO, Al_2O_3), microcline (K_2O), Amelia Albite (Na_2O), synthetic Ti (TiO_2), and synthetic Cr (Cr_2O_3). Internal uncertainties (2σ) based on counting statistics are ≤2 % for SiO_2, Al_2O_3, and CaO; ≤5 % for FeO, Na_2O, K_2O, TiO_2, Cr_2O_3, and MgO; and ≤10 % for MnO.

LA-ICP-MS analysis

Trace element analyses were performed using a ThermoFinnegan Element2 high-resolution ICP-MS (Thermo Scientific, Bremen, Germany) coupled to a New Wave UP213 Nd:YAG laser ablation system (ESI, Portland, OR, USA). Operating conditions (Table 1) were 5 Hz pulse rate and 40 μm spot size for a corresponding fluence of 10–12 J cm^{-2}. Background signals were monitored for ~60 s. For the final 20 s the laser was on and shuttered to stabilize power output prior to ablation of the standard and unknowns. The sample ion signals were subsequently analyzed for ~60 s during ablation. Repeated measurements (two prior and two subsequent to the unknowns) of the external standard NIST SRM 612 glass bracketed every analysis of ten or fewer Trinitite samples. This method was facilitated by the UP213 sample chamber, which accommodated simultaneously both the sample and NIST SRM 612 standard wafer. Trace element concentrations, internal uncertainties (1σ), and limits of detection were determined using the program *GLITTER*©, which allows for the reduction of time-resolved signal analysis ([23]; http://www.glitter.gemoc.com). Pu and U isotopic ratios were calculated based on average background-subtracted count rates of monitored isotopes using the method of Wallace et al. [16].

Results

Major and trace elements

Major and trace element results from 228 EMP analyses and corresponding LA-ICP-MS measurements are summarized in Table 2 and Figs. 2, 3, and 4. Results for individual analyses are listed in Supplemental Table S1. Typical Trinitite glass is composed predominantly of SiO_2 (58–70 wt%), with variable amounts of Al_2O_3 (10–20 wt%), CaO (4–15 wt%), K_2O (2–6 wt%), and FeO (1–5 wt%). Subgroups of Trinitite glass are defined by the influence of common precursor minerals present within the desert sand at GZ, including high-Si regions (>80 wt% SiO_2) due to localized quartz melting. Ca-rich Trinitite (>10 wt% CaO) and K-rich glass (>6 wt% K_2O) are likely attributable to the melting of calcite and K-feldspar, respectively (Fig. 2a). High-Fe glass (>5 wt% FeO) is typically dark in plane polarized light, and some Fe-rich regions are centered near anhedral magnetite grains. The high temperature produced by the nuclear blast (>1470 °C; [15]) vitrified most of the precursor desert minerals. However, relict grains of quartz are common, with fewer K-feldspar grains, zircons, and trace other minerals [24]. Micro-XRF maps reveal these relict quartz and K-feldspar regions (yellow and blue, respectively, in Fig. 1) are 0.5–2 mm in size.

High-Ca regions (>10 wt% CaO) are in general characterized by higher U and Pu contents compared to lower-Ca regions (Fig. 3a–b), which corroborates similar trends observed in Trinitite by Wallace et al. [16] and Fahey et al. [9]. For most analyses with high-Ca contents, the corresponding U abundances are consistent with that of un-melted sand

Table 2 Average major element oxide (wt%), and trace element abundances (ppm with associated 1σ uncertainty) for common varieties of Trinitite glass

	Typical glass	High-Si	High-Ca	High-K	High-Fe
n*	18	2	9	12	4
FeO	2.27	1.72	2.40	0.63	13.2
MnO	0.08	0.03	0.06	0.01	0.65
Na_2O	2.68	1.27	1.24	3.31	1.57
Al_2O_3	15.0	4.80	9.93	18.5	9.88
MgO	1.13	0.46	1.10	0.18	0.91
K_2O	4.32	2.67	1.75	9.74	2.36
CaO	6.87	3.09	24.5	1.29	6.27
TiO_2	0.42	0.25	0.35	0.07	13.4
SiO_2	66	85	58	66	49
Cr_2O_3	0.01	0.00	0.01	0.00	0.02
SUM	98.83	99.16	99.04	99.43	97.66
Co	5.25 ± 0.30	*b.d.*	5.31 ± 0.25	2.41 ± 0.20	*b.d.*
Cu	14.0 ± 1.0	6.00 ± 0.52	16.0 ± 1.4	4.38 ± 0.65	45.6 ± 7.8
Ga	12.7 ± 0.6	*b.d.*	11.7 ± 0.5	13.2 ± 0.8	*b.d.*
Rb	177 ± 7	39.8 ± 4.0	59.4 ± 3.8	371 ± 22	68.0 ± 5.8
Sr	339 ± 48	112 ± 16	372 ± 41	150 ± 15	257 ± 39
Y	10.5 ± 1.0	5.14 ± 0.44	14.7 ± 1.0	1.15 ± 0.14	21.8 ± 1.8
Zr	54.8 ± 3.0	20.9 ± 1.6	67.0 ± 4.8	5.67 ± 0.36	89.4 ± 6.0
Nb	9.68 ± 0.78	2.42 ± 0.18	7.97 ± 0.68	0.94 ± 0.08	81.8 ± 4.4
Sn	1.49 ± 0.28	0.60 ± 0.16	1.05 ± 0.26	1.13 ± 0.32	1.67 ± 0.33
Cs	5.27 ± 0.26	1.17 ± 0.05	1.58 ± 0.09	11.4 ± 0.6	2.24 ± 0.15
Ba	1022 ± 46	243 ± 8	639 ± 26	1891 ± 86	637 ± 31
La	18.4 ± 0.8	7.22 ± 0.25	22.2 ± 1.0	4.54 ± 0.24	20.1 ± 1.0
Ce	39.0 ± 1.3	13.6 ± 0.45	40.2 ± 1.9	2.68 ± 0.12	44.3 ± 2.2
Pr	4.13 ± 0.16	1.72 ± 0.07	4.83 ± 0.22	0.31 ± 0.02	4.63 ± 0.23
Nd	14.5 ± 0.7	6.33 ± 0.26	17.9 ± 0.9	1.15 ± 0.09	17.6 ± 0.9
Sm	2.63 ± 0.17	1.10 ± 0.09	3.26 ± 0.22	0.29 ± 0.04	3.66 ± 0.29
Eu	0.72 ± 0.07	0.31 ± 0.02	0.76 ± 0.05	0.56 ± 0.05	0.79 ± 0.06
Gd	2.24 ± 0.14	1.00 ± 0.07	2.77 ± 0.15	0.24 ± 0.05	3.42 ± 0.22
Tb	0.32 ± 0.03	0.14 ± 0.02	0.42 ± 0.03	0.04 ± 0.02	0.51 ± 0.04
Dy	1.84 ± 0.12	0.82 ± 0.05	2.54 ± 0.16	0.25 ± 0.03	3.74 ± 0.25
Ho	0.36 ± 0.03	0.18 ± 0.01	0.51 ± 0.03	0.04 ± 0.01	0.77 ± 0.05
Er	1.11 ± 0.08	0.54 ± 0.04	1.51 ± 0.10	0.16 ± 0.02	2.38 ± 0.17
Tm	0.18 ± 0.02	0.07 ± 0.01	0.24 ± 0.02	0.02 ± 0.01	0.40 ± 0.03
Yb	1.23 ± 0.10	0.54 ± 0.05	1.76 ± 0.12	0.17 ± 0.03	2.96 ± 0.20
Lu	0.19 ± 0.02	0.09 ± 0.01	0.25 ± 0.02	0.02 ± 0.01	0.45 ± 0.04
Hf	2.62 ± 0.13	1.19 ± 0.06	3.41 ± 0.17	0.26 ± 0.02	5.16 ± 0.26
Ta	0.56 ± 0.04	0.17 ± 0.01	0.58 ± 0.04	0.17 ± 0.02	5.28 ± 0.22
W	0.58 ± 0.06	0.18 ± 0.02	0.57 ± 0.06	0.07 ± 0.02	1.43 ± 0.11
Pb	19.1 ± 1.0	2.35 ± 0.12	9.45 ± 0.57	59.9 ± 3.2	20.7 ± 1.2
Th	7.97 ± 0.41	2.87 ± 0.10	8.86 ± 0.37	0.50 ± 0.03	7.42 ± 0.34
U	1.93 ± 0.09	0.92 ± 0.06	3.41 ± 0.16	0.60 ± 0.03	4.24 ± 0.43
Pu cps	198 ± 12	198 ± 14	913 ± 25	95	180 ± 14
$^{240}Pu/^{239}Pu$	0.017 ± 0.021	0.009	0.022	0.004	0.034 ± 0.033
$^{235}U/^{238}U$	0.009 ± 0.002	0.005 ± 0.001	0.008 ± 0.001	0.171	0.009 ± 0.001

*n** representative number of analyses used to calculate the average; *b.d.* below detection limit

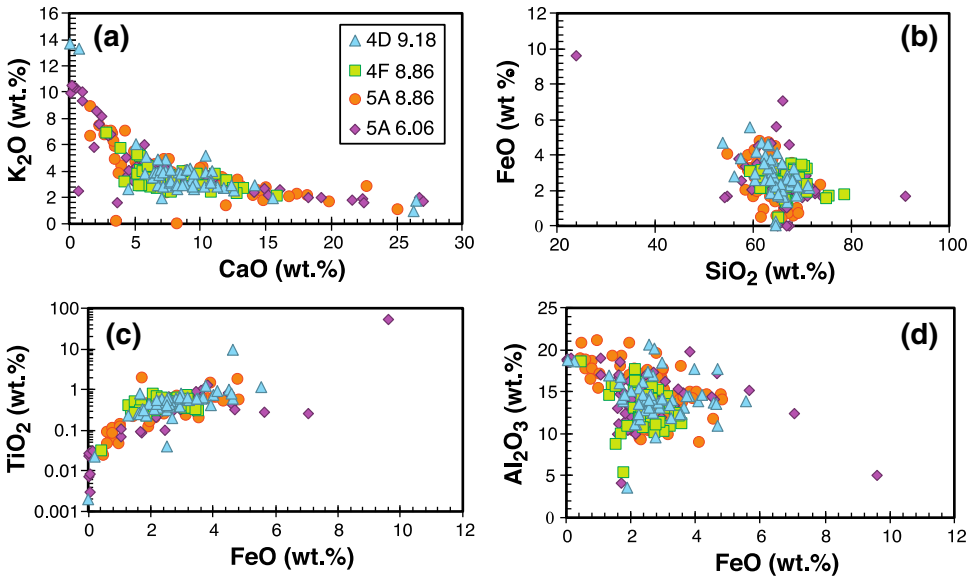

Fig. 2 Major element variation diagrams of Trinitite glass. **a** Trends toward high CaO and high K_2O reflect calcite and K-feldspar contributions, respectively. **b** Trinitite glass consists predominantly of SiO_2. **c** FeO and TiO_2 wt% abundances are positively correlated. **d** High Al_2O_3 contents at corresponding low FeO wt% abundances indicates feldspar dominating the minor element signature in some analyses. Uncertainties in EMP analyses are smaller than the size of symbols shown

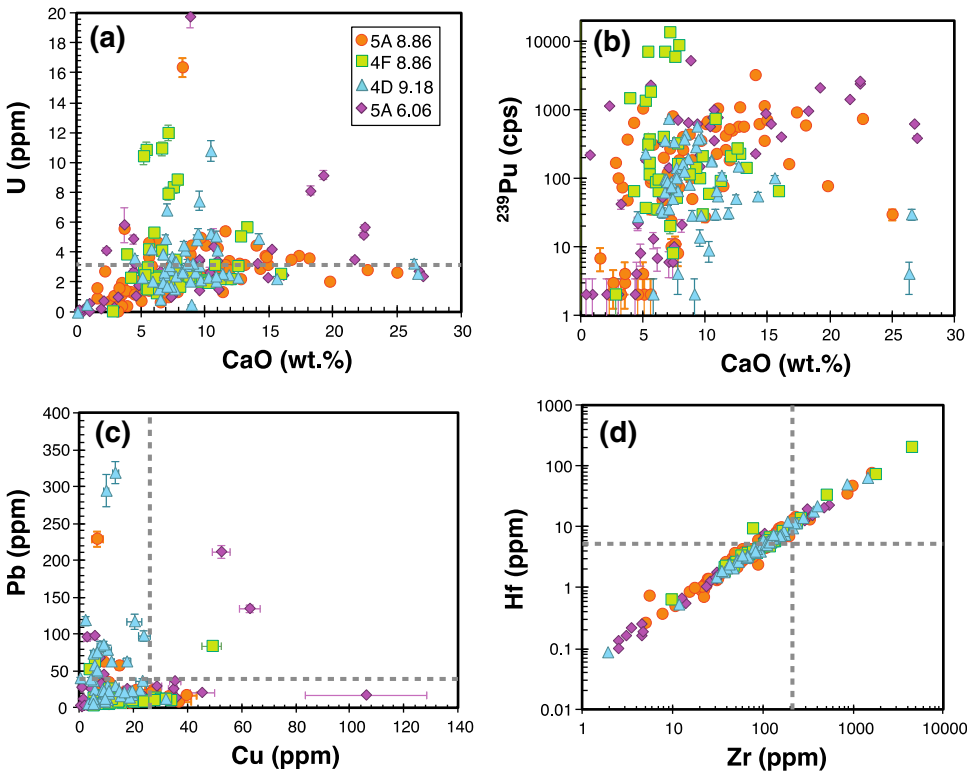

Fig. 3 Major and trace element diagrams of Trinitite glass analyses. **a** U concentrations in high Ca regions are consistent with unmelted Trinitite sand [4]. U enrichment is more likely to reflect anthropogenic input. **b** There also appears to be a positive correlation between Pu and CaO. The ^{239}Pu ion signal, counts per second (cps), is used as a proxy for the absolute abundances of Pu. The latter cannot be calculated since it is not contained within the NIST SRM 612 standard; **c** Pb (ppm) versus Cu (ppm). **d** Constant Hf/Zr ratio (0.045 ± 0.002) indicates zircon control for these elements. *Dashed gray lines* in all plots indicate the pertinent concentrations for those elements within un-melted arkosic sand [4]; moreover, the abundance of Pu in the sand (Fig. 3b) is zero prior to the Trinity nuclear detonation

(i.e., ~3.2 ppm; [4]), indicating a natural source (Fig. 3a). Many elements show orders of magnitude variation but with few correlations, such as the abundances of Cu versus Pb (Fig. 3c); both elements are abundant in Trinitite containing red surface inclusions [4]. In addition, both Zr and Hf contents define orders of magnitude variation at a constant Zr/Hf ratio of 0.045 (Fig. 3d), which is consistent and attributable to the precursor, low modal amount (<1 %) of zircon within the sand at Trinity.

The average arkosic sand from the Trinity site [4] exhibits a concave up rare earth element (REE) pattern (chondrite normalized), with a negative light REE (LREE) slope, slight negative Eu-anomaly, and flat heavy REE (HREE) profile (Fig. 4). The majority of individual glass analyses reported here (190 of 228 measurements) exhibit REE profiles similar to that for the un-melted sand, although absolute concentrations vary by as much as a factor of three. The dominant factors controlling the REE

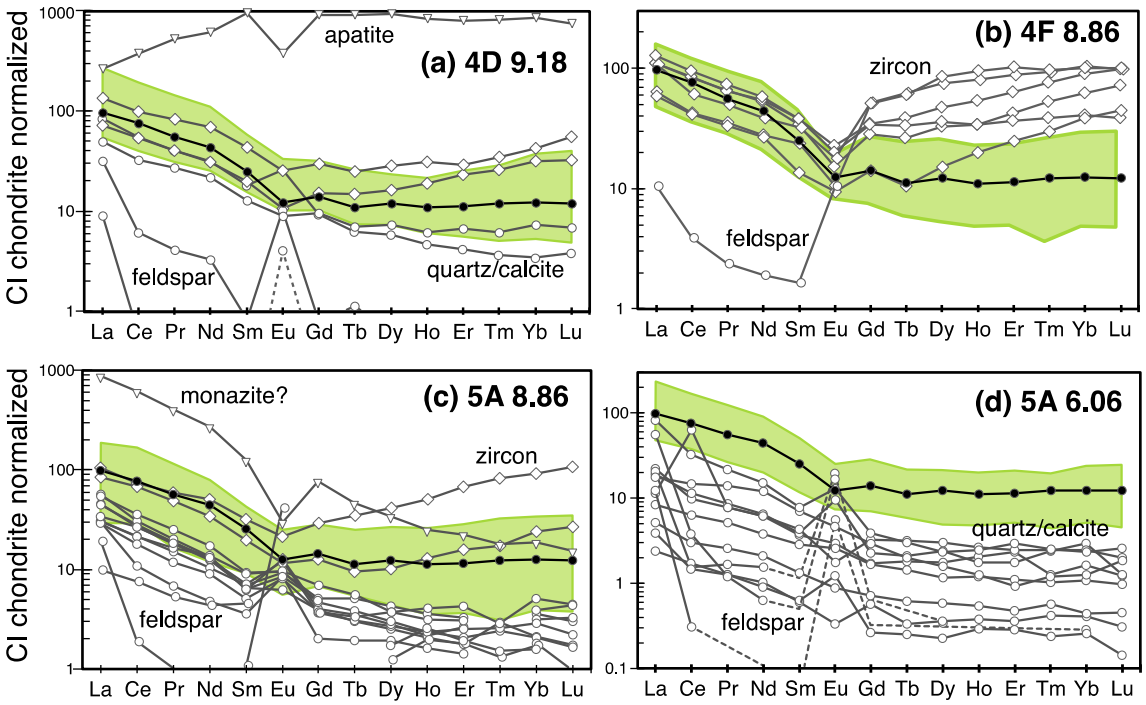

Fig. 4 Chondrite normalized rare earth element profiles for the four samples investigated here compared to un-melted sand (*bold black line with solid circles*) from the sandy side of Trinitite [4]. The *green* field represents the majority of analyses, which define patterns that are subparallel to the un-melted sand. *Gray lines* with unfilled symbols represent patterns for more 'unusual' analyses that reflect signatures for specific mineral contributions

budgets of bulk Trinitite are believed to be the variable contributions by quartz, feldspars, and trace amounts of accessory minerals such as zircon, monazite, and apatite [4]. Significant plagioclase contribution to Ca-rich regions (>10 wt% CaO) is reflected by a positive Eu-anomaly in chondrite normalized REE-patterns and overall lower concentrations (i.e., diluted REE profile; Fig. 4a, c, d). In general, analyses exhibiting the lowest REE chondrite normalized values are characterized by the highest K abundances. Moreover, some Trinitite analyses have typical LREE and elevated HREE signatures, which may reflect zircon contributions; these analyses are also characterized by elevated Zr contents. Other identifiable mineral influences include apatite by the REE-enriched (~1000× chondrite) profile (Fig. 4a), and monazite/apatite by the steep negative REE profile (Fig. 4c).

Cross-section transects

Three transects were conducted across each sample, with an average spacing of 0.24–1.0 mm per sample, and a maximum depth of ~10 mm (Fig. 1). The average distance between EMP points in the upper 2 mm was ~0.3 mm, and average spacing increased with depth (from glassy top side) due to increasing vesicle and mineral fragment abundances. Within each transect, the proportion of silicate mineral fragments increased with depth. In general, vesicle size decreases with increasing depth. There is also a tendency for vesicles to be ovoid and elongated parallel to the sample surface. In an investigation of a single Trinitite sample, Sharp et al. [18] noted three distinct regions, comprising an uppermost glassy layer, middle transitional-glassy layer, and lower, relatively un-melted mineral fragments. In this study, there does not appear to be a layer with significant un-melted material, but the uppermost glass-dominated layer is present and covers a transitional mixture of glass and mineral fragments. In each vertically oriented sample, this transition begins at ~2 mm depth.

In Fig. 5, only analyses with typical Trinitite REE profiles are shown (see discussion section). The upper 2 mm is most likely to contain major U enrichment, with these enriched regions found in high alpha track density regions, although this feature is not prevalent in every sample (Fig. 5e–g). The glassy portion of obliquely cut 5A 6.06 also records U enrichment in the outer 2 mm (Fig. 5h). The calculated $^{240}Pu/^{239}Pu$ ratio of the Gadget is 0.0128 [8]; however, recent studies of Trinitite measured $^{240}Pu/^{239}Pu$ ratios ranging between 0.0176 [9], ~0.021 [e.g., 16] and ~0.026 (average of [18]). This fingerprint dominates the upper 2 mm of Trinitite samples investigated here (Fig. 5i–l), and the ratio increases slightly with depth in sample 4D 9.18. However, in each sample a weapons grade $^{240}Pu/^{239}Pu$ ratio is also identified at depths up to ~10 mm.

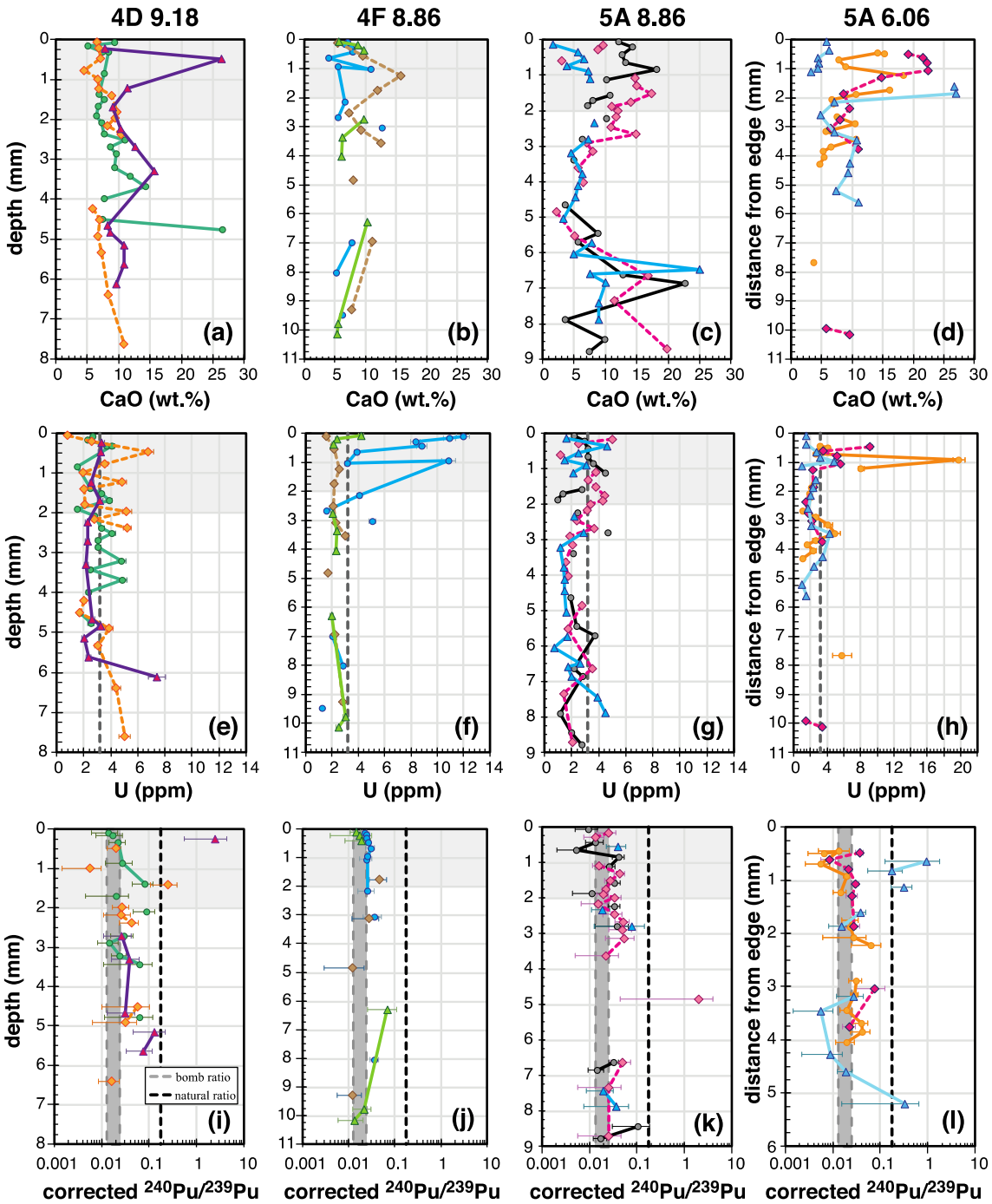

Fig. 5 Analytical transects through the samples. In (**a**–**d**), regions of high CaO are present at varying depths within samples. In vertical cross-sections, the most significant deviations are recorded in the upper 2 mm. The *dashed line* in (**e**–**h**) represents the concentration of U in un-melted sand (U = 3.2 ppm; [4]). In (**i**–**l**), the *thick gray bar* (enveloped by the *dashed lines*) represents the range in bomb Pu signatures for the Trinity device [9, 16, 18], while the *dashed line* represents the natural fallout Pu ratio for the region surrounding GZ [25]. A bomb-like signature is found at depths >6 mm in all vertically oriented samples. Uncertainties are reported as relative standard deviations (2σ)

Discussion

Mineralogical control on Trinitite composition

The textural and chemical heterogeneity of Trinitite, as demonstrated in Figs. 2, 3, and 4, has been previously reported [4, 12, 16]. Glass composition is strongly influenced by precursor sand components (e.g., calcite influence on CaO abundance in Fig. 2a), which can potentially mask anthropogenic contributions. A major goal of nuclear forensics is to distinguish between anthropogenic components and device signatures within PDMs. Bellucci et al. [4]

identified anthropogenic contributions on the basis of deviations from expected trends in mineral control lines, and comparing trace element abundances within Trinitite to those for un-melted sand composition. An alternative, simpler approach adopted here is to utilize the characteristic chondrite normalized REE profile of un-melted Trinitite to quickly identify characteristic minerals present in the desert sand at GZ (Fig. 4). As shown in Fig. 4, the majority of chondrite normalized REE profiles of Trinitite glass are subparallel to the un-melted sand composition, and vary only relative to absolute abundances. The latter feature can be attributed to dilution from predominant REE-poor phases present in the sand, primarily quartz, calcite, and feldspar. Specific REE patterns can also be attributed to strong influence by specific mineral components. For example, plagioclase feldspar is identified by a positive Eu-anomaly and slight LREE enrichment at lower chondrite normalized values (Fig. 4). In relation to controlling the REE budget of Trinitite, trace accessory minerals such as apatite, monazite, and zircon are characterized by high concentrations of REEs; i.e., apatite and monazite are a major source of the LREEs and Th, whereas zircon controls the budget of the HREEs, U, Hf, and Zr. The Hf/Zr ratio of 0.045 (Fig. 3d) is consistent with natural zircon containing $\sim$60 wt% ZrO_2 and $\sim$2–3 wt% HfO_2. Other accessory minerals present in the precursor desert sand, such as ilmenite, will exert an important control on the distribution of Ta and Nb abundances within Trinitite. Therefore, on the basis of the trace element abundances and resulting patterns (e.g., Fig. 4), it is important to identify the trace element signatures of accessory minerals that are present to minimize their inaccurate attribution to device components.

Hence, we have applied this mineral component 'filter' to all of the high spatial resolution analyses conducted here. The remaining analyses display remarkable homogeneity as the variation in REE abundances is reduced to within an order of magnitude. This relatively rapid 'filtering' method was used in Fig. 5, where only samples with subparallel REE profiles to un-melted Trinitite are shown. Thus, other explanations must be considered for regions where, for example, U abundance is not controlled by melted minerals (e.g., monazite). Of the three vertical cross-sections, U enrichment was found only in sample 4F 8.86 (Fig. 5f), in the upper 2 mm glassy portion. The obliquely cut sample 5A 6.06 also exhibited U enrichment limited to the glassy section. The limited occurrence and presence of U only at the surface of Trinitite suggests an anthropogenic source, likely from the Gadget device tamper [7]. Also, these two samples formed >74 m (4F 8.86) and 51 m (5A 6.06) from GZ, which reflect the heterogeneous distribution of device components. Pu concentrations, using Pu ion signals as a proxy, did not reveal systematic variations with depth. For each sample, the highest Pu abundance was typically found in the upper 2 mm, although deeper analyses often yielded regions with similar ion signal intensities. Additionally, regions of high Pu abundance below 2 mm depth were never more than a factor of two higher than Pu yields from the upper 2 mm. Thus, similar degrees of Pu enrichment occur at variable depths within Trinitite cross-sections.

The petrography and vesicle morphology of the three vertical thin sections supports an origin by in situ melting [12, 15, 17] and subsequent deposition of fallback particles [17, 18]. The dichotomy between an upper glassy layer with few, relatively large vesicles, and a highly vesicular lower region has been observed in other Trinitite samples [18, 26]. The heterogeneous distribution of pooled glass is demonstrated by the difference in thickness between this study, where it is $\sim$2 mm thick, the 2.5 mm thick glass of Giuli et al. [26], and the 1 mm thick glassy region of Sharp et al. [18]. In addition, Trinitite was not created as a uniform, flat layer of glass. Photos of the desert surface shortly after the blast reveals a patchy network of glass with centimeter scale voids [c.f., 8]. As a result, many Trinitite fragments are rounded, and the glassy, devolatilized layer may be present on the sides of some samples. Further studies of vesicle development and mineral vitrification in nuclear blast melt may be aided by investigation of synthetic/surrogate Trinitite-like nuclear debris [27].

Implications of plutonium distribution

As discussed previously, Trinitite is thought to have formed by a combination of in situ melting and deposition of debris cloud material [4, 17, 18]. The uppermost surface would be quenched to a semi-solid glass by the air. This would then trap subsurface heat at temperatures above the boiling point of water for a sufficiently long period of time to form bubbles in the molten glass. This formation agrees with the glassy layer of Trinitite blast melt, observed vesicle distribution, and non-mineral-associated contribution of U to the uppermost surface (Fig. 5e–h). In contrast, the identification of a weapons grade Pu signature at depth (Fig. 5i–l) is more difficult to reconcile with these methods of formation. Material from the debris cloud must have penetrated to depths >6 mm, which is unlikely if only in situ melting dominated below 2 mm depth.

The presence of supergrade Pu isotope signatures at depth requires thorough disturbance and mixing of the local sand during the blast. The samples investigated here originated between 50 and 370 m (the maximum extent of Trinitite) from GZ. At a radial distance of 410 m, the peak pressure of the excess velocity was 45.2 psi [28]. Focused on sand-sized particles, this pressure would be sufficient to disturb the upper surface surrounding GZ. By comparison,

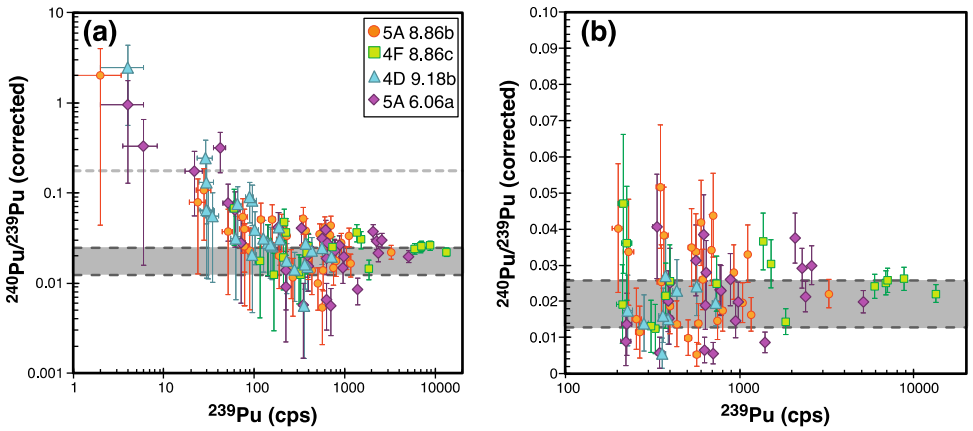

Fig. 6 ^{239}Pu count rates from LA-ICP-MS analyses compared to calculated ^{240}Pu/^{239}Pu ratios (corrected using the method of [16]). **a** Analyses recording higher ^{239}Pu ion signals (>1000 cps) are less variable and are more likely to reflect a nuclear device signature (*thick gray bar*). **b** Portion of (**a**) with a lower cutoff of 200 cps ^{239}Pu. Uncertainties are relative standard deviation (2σ). *Light gray dashed line* in plot 6a represents the Pu isotope composition for the natural background at Trinity in 1978 [25]

earthen embankments up to 730 m from GZ were also scoured away [28]. We propose that the upper surface was briefly and vigorously mixed to depths of at least 1 cm, with variation dependent upon proximity to GZ and local topography. The majority of device-related material would not be entrained in this zone, as it would remain in the vapor cloud for several seconds. In-situ melting and heating by debris cloud material would then proceed. Mixing during initial melting would allow the degree of homogenization observed in the primary Trinitite glass composition.

In-situ LA-ICP-MS analyses with the highest ion signals of ^{239}Pu yield calculated isotopic ^{240}Pu/^{239}Pu ratios that range between 0.012 and 0.026, which correspond to those for the Trinity device (Fig. 6). A negative correlation exists between ^{240}Pu/^{239}Pu and ^{239}Pu for ion signals <1000 cps (counts per second). In particular, there is a linear lower limit of ^{240}Pu/^{239}Pu for samples with <1000 cps. The counting statistics for the measurement of extremely low ^{240}Pu ion signals ($n = 1$–2 cps) renders the calculated ^{240}Pu/^{239}Pu ratios for such analyses essentially invalid. Analysis of the NIST SRM 612 standard wafer, which does not contain Pu, frequently yielded ^{239}Pu ion signals of 2 cps or more. Thus, caution must be taken when interpreting the Pu isotope ratios as a function of measured ion signals. For example, the increasing ^{240}Pu/^{239}Pu ratio with decreasing count rates (Fig. 6) is not attributable to mixing between the bomb-device and natural background [25]. The "natural ^{240}Pu/^{239}Pu ratio" of 0.176 within the region of Alamogordo, NM represents the atom ratio for global fallout as a result of two decades of nuclear testing [25, 28], which had not yet occurred before the Trinity test. It has also been demonstrated that vitrification and the arid environment at the Trinity site has resulted in no observable leaching of radioactive components into the surrounding environment [12]. An alternative explanation is that natural fallout and bomb-related Pu may have mixed during petrographic thin section preparation of the Trinitite samples as water was used in their fabrication. However, the validity of this interpretation needs to be further investigated.

Conclusions

Trinitite is heterogeneous by nature, and contributions by various mineral phases present within the desert sand at GZ during melting after the nuclear explosion are identifiable using high spatial resolution analysis. The major and trace element signatures of common minerals found in arkosic sand are used as a rapid filtering method to remove their natural, geological background contribution to the Trinitite glass composition. The resulting chemical distributions demonstrate a higher degree of homogeneity for trace elements than previously interpreted, and anthropogenic contributions are easier to identify. Pu from the device, as interpreted from the supergrade ^{240}Pu/^{239}Pu signature, is found deeper (up to ~1 cm) within Trinitite than previously described. Incorporation of device Pu requires rapid mixing of local sand by the initial blast wave, prior to and possibly during initial melting.

Acknowledgments We thank Dr. Ian Steele for assistance with EMP analyses at the University of Chicago. Sandy Dillard of the Brazos Valley Petrographic Thin Section Services Lab (Bryan, Texas) is thanked for production of thin sections of Trinitite. We also wish to thank the Center for Environmental Science and Technology at the University of Notre Dame for use of the μ-XRF. This manuscript was improved by comments from two anonymous reviewers, and we thank Zsolt Revay for editorial handling. This research is funded by DOE/NNSA grant PDP11-40/DE-NA0001112.

References

1. Mayer K, Wallenius M, Fanghänel T (2007) Nuclear forensic science—from cradle to maturity. J Alloy Compd 444–445:50–56. doi:10.1016/j.jallcom.2007.01.164
2. Mayer K (2013) Expand nuclear forensics. Nature 503:461–462
3. Hermes RE, Strickfaden WB (2005) A new look at trinitite. Nucl Weapons J 2:2–7
4. Bellucci JJ, Simonetti A, Koeman EC, Wallace C, Burns PC (2014) A detailed geochemical investigation of post-nuclear detonation trinitite glass at high spatial resolution: delineating anthropogenic vs. natural components. Chem Geol 365:69–86. doi:10.1016/j.chemgeo.2013.12.001
5. Eppich GR, Knight KB, Jacomb-Hood TW, Spriggs GD, Hutcheon ID (2014) Constraints on fallout melt glass formation from a near-surface nuclear test. J Radioanal Nucl Chem 302:593–609. doi:10.1007/s10967-014-3293-9
6. Schlauf D, Siemon K, Weber R, Esterlund RA, Molzahn D, Patzelt P (1997) Trinitite redux: comment on "'Determining the yield of the Trinity nuclear device via gamma-ray spectroscopy,'" by David Atkatz and Christopher Bragg [Am. J. Phys. 63, 411–413 (1995)]. Am J Phys 65:1110–1112
7. Rhodes R (1986) The making of the atomic bomb. Simon and Schuster, New York
8. Parekh PP, Semkow TM, Torres MA, Haines DK, Cooper JM, Rosenberg PM, Kitto ME (2006) Radioactivity in Trinitite six decades later. J Environ Radioact 85:103–120. doi:10.1016/j.jenvrad.2005.01.017
9. Fahey AJ, Zeissler CJ, Newbury DE, Davis J, Lindstrom RM (2010) Postdetonation nuclear debris for attribution. P Natl Acad Sci 107:20207–20212. doi:10.1073/pnas.1010631107
10. Staritzky E (1950) Thermal effects of atomic bomb explosions on soils at Trinity and Eniwetok. Los Alamos Sci Lab 21:1–21
11. Pettijohn FJ (1963) Chapter S: the chemical composition of sandstones—excluding carbonate and volcanic sands. In: Fleischer M (ed) Data of geochemistry, 6th edn. US Geol Soc Prof Paper 440-S, Washington
12. Eby GN, Hermes R, Charnley N, Smoliga JA (2010) Trinitite—the atomic rock. Geol Today 26:180–185
13. Koeman EC, Simonetti A, Chen W, Burns PC (2013) Oxygen isotope composition of trinitite postdetonation materials. Anal Chem 85:11913–11919. doi:10.1021/ac402757p
14. Storms B (1965) Trinity. Atom 2(8):1–34
15. Ross CS (1948) Optical properties of glass from Alamogordo, New Mexico. Am Mineral 33:360–362
16. Wallace C, Bellucci JJ, Simonetti A, Hainley T, Koeman EC, Burns PC (2013) A multi-method approach for determination of radionuclide distribution in trinitite. J Radioanal Nucl Chem 298:993–1003. doi:10.1007/s10967-013-2497-8
17. Belloni F, Himbert J, Marzocchi O, Romanello V (2011) Investigating incorporation and distribution of radionuclides in trinitite. J Environ Radioact 102:852–862. doi:10.1016/j.jenvrad.2011.05.003
18. Sharp N, McDonough WF, Ticknor BW, Ash RD, Piccoli PM, Borg DT (2014) Rapid analysis of trinitite with nuclear forensic applications for post-detonation material analyses. J Radioanal Nucl Chem. doi:10.1007/s10967-014-3285-9
19. Bellucci JJ, Simonetti A (2012) Nuclear forensics: searching for nuclear device debris in trinitite-hosted inclusions. J Radioanal Nucl Chem 293:313–319. doi:10.1007/s10967-012-1654-9
20. Bellucci JJ, Simonetti A, Wallace C, Koeman EC, Burns PC (2013) Isotopic fingerprinting of the world's first nuclear device using post-detonation materials. Anal Chem 85:4195–4198. doi:10.1021/ac400577p
21. Bellucci JJ, Simonetti A, Wallace C, Koeman EC, Burns PC (2013) Lead isotopic composition of trinitite melt glass: evidence for the presence of Canadian industrial lead in the first atomic weapon test. Anal Chem 85:7588–7593. doi:10.1021/ac4016648
22. >Bellucci JJ, Wallace C, Koeman EC, Simonetti A, Burns PC, Kieser J, Port E, Walczak T (2013) Distribution and behavior of some radionuclides associated with the Trinity nuclear test. J Radioanal Nucl Chem 295:2049–2057. doi:10.1007/s10967-012-2201-4
23. van Achterbergh E, Ryan CG, Jackson SE, Griffin WL (2001) Data reduction software for LA-ICP-MS: appendix. In: Sylvester PJ (ed) Laser ablation-ICP-mass spectrometry in the earth sciences: principles and applications. Mineralogical Association of Canada, Short Course Series, pp 239–243
24. Mana S, Simonetti A, Koeman EC, Donohue PH, Burns PC (2014) Detailed textural, geochemical, and U-Pb geochronological investigation of detrital zircons within Trinitite post-detonation material. Geol Soc Am Abs Prog 46:103
25. Douglas RL (1978) Levels and distribution of environmental plutonium around the Trinity site. EPA Tech Note ORP/LV-78-3:1–51
26. Giuli G, Pratesi G, Eeckhout SG, Koeberl C, Paris E (2010) Iron reduction in silicate glass produced during the 1945 nuclear test at the Trinity site (Alamogordo, New Mexico, USA). Geol Soc Am Spec Publ 465:653–660. doi:10.1130/2010.2465(32)
27. Molgaard JJ, Auxier JD, Giminaro AV, Oldham CJ, Cook MT, Young SA, Hall HL (2015) Development of synthetic nuclear melt glass for forensic analysis. J Radioanal Nucl Chem. doi:10.1007/s10967-015-3941-8
28. Bainbridge KT (1976) Trinity (No. LA-6300-H). Los Alamos Scientific Laboratory, Los Alamos